

Final Technical Report

NEHRP/USGS Award Number: G16AP00007

Interseismic coupling of the north San Francisco Bay faults from InSAR, GPS, and seismic data: collaborative research with UC Berkeley and USGS Menlo Park

Roland Bürgmann, Professor
Berkeley Seismological Laboratory
University of California, Berkeley
215 McCone Hall
Berkeley, CA 94720-4767
Tel: (510) 643-9545; Fax: (510) 643-5811
Email: burgmann@seismo.berkeley.edu

Robert Nadeau, Researcher
Berkeley Seismological Laboratory
University of California, Berkeley
211 McCone Hall
Berkeley, CA 94720-4767
Tel: (510) 643-3980; Fax: (510) 643-5811
Email: nadeau@seismo.berkeley.edu

Term covered by this award: 12/01/2015 – 05/31/2018

ABSTRACT:

The detailed spatial variations of strain accumulation and creep on major faults in the northern San Francisco Bay Area (North Bay), which are important for seismic potential and evaluation of natural hazards, remain poorly understood. Here we combine interferometric synthetic aperture radar (InSAR) data from the ERS-1/2 and Envisat satellites between 1992 and 2010 with continuous and campaign GPS data to obtain a high spatial and temporal coverage of ground deformation of the North Bay. The SAR data from both ascending and descending orbits are combined to separate horizontal and vertical components of the deformation. We jointly invert the horizontal component of the mean velocities derived from these data to infer the deep strike-slip rates on major locked faults. We use the estimated deep rates to simulate the long-wavelength deformation due to interseismic elastic strain accumulation along these locked faults. After removing the long-wavelength signal from the InSAR horizontal mean velocity field, we estimate fault-parallel surface creep rates of up to 2 mm/yr along the central section of the Rodgers Creek fault and surface creep rates ranging between 2 and 4 mm/yr along the Concord fault. No surface creep is geodetically resolved along the West Napa and Green Valley fault zones. We identified characteristically repeating earthquakes on the Rodgers Creek fault, the West Napa fault, the Green Valley fault and the Concord fault. Nontectonic deformation in the Geysers geothermal field (maximum subsidence of ~ 17 mm/yr) and in Late Cenozoic basins (Rohnert Park and Sonoma basins) are also observed, likely due to hydrological and sediment-compaction processes, respectively.

REPORT:

1. 1. Introduction

This project is focused on analyzing and modeling two decades of regional crustal deformation data associated with the San Andreas, Rodgers Creek-Maacama, West Napa, and Concord-Green Valley-Bartlett Springs Faults, in the northern San Francisco Bay Area (North Bay). This effort addresses the seismic potential and natural hazard presented by these major faults through the combined use of space geodesy and seismology. Geodetic measurements provide information on the nature of elastic strain accumulation and release on seismogenic faults, their long-term slip and creep rates, and variations of those parameters in space and time, while seismicity will provide constraints on the faults' structure and creep at depth. The results presented in this report are published in *Xu et al.* [2018].

The San Andreas Fault System in the northern San Francisco Bay Area (North Bay) consists of four major sub-parallel strands, the northern San Andreas, Rodgers Creek-Maacama, West Napa, and Concord-Green Valley-Bartlett Springs fault zones (Fig. 1). Several moderate to large earthquakes have occurred on these faults during the past century. In 1906, a M_w 7.8 earthquake took place on the northern San Andreas fault with a total rupture length of ~ 470 km [*Thatcher et al.*, 1997] causing significant damage to the city of San Francisco. In 1969, two damaging moderate magnitude (M_L 5.6 and M_L 5.7) earthquakes occurred near the city of Santa Rosa, likely on the Healdsburg section of the Rodgers Creek fault [*Wong and Bott*, 1995]. More recently, a M_w 6 earthquake ruptured the West Napa fault on August 24, 2014, causing significant economic damage in the region [e.g., *Earthquake Engineering Research Institute*, 2015]. No major earthquakes have occurred during the historical record on either the Maacama fault, the Concord-Green Valley fault or the Bartlett Springs fault, despite the accumulation of a slip deficit that is now likely large enough to generate $\sim M_w$ 7 earthquakes on these faults [*Freymueller et al.*, 1999; *Murray et al.*, 2014]. Compared to the well-studied faults in the central Bay Area [*Burgmann et al.*, 2000; *d'Alessio et al.*, 2005; *Shirzaei and Bürgmann*, 2013; *Chaussard et al.*, 2015a], the spatial variations of strain accumulation and creep on major faults in the North Bay remain poorly understood.

Interseismic deformation and fault creep have been primarily estimated from Global Positioning System (GPS) and alignment array data in the North Bay. *Freymueller et al.*, [1999] simultaneously estimated the locking depths and deep slip rates of the northern San Andreas fault, Maacama fault and Bartlett Springs fault using 2-D models. They found deep slip rates of $17.4^{+2.5}_{-3.1}$ mm/yr, $13.9^{+4.1}_{-2.8}$ mm/yr, $8.2^{+2.1}_{-1.9}$ mm/yr and locking depths of $14.9^{+12.5}_{-7.1}$ km, $13.4^{+7.4}_{-4.8}$ km, and 0 km for the northern San Andreas fault, Maacama fault and Bartlett Springs fault, respectively. Based on the analysis of both campaign and continuous GPS data collected between 1992 and 2000, *Prescott et al.*, [2001] estimated a 20.8 ± 1.9 mm/yr deep slip rate on the northern San Andreas fault, 10.3 ± 2.6 mm/yr on the Rodgers Creek fault, and 8.1 ± 2.1 mm/yr on the Concord-Green Valley fault, respectively. The estimated locking depths are 11 km, 12 km and 14 km for the northern San Andreas fault, Rodgers Creek fault and Green Valley fault, respectively. *Prescott et al.*, [2001] found a slightly higher slip rate for the Green Valley fault than that estimated from geologic data and the inferred slip rate for the SAF is somewhat lower than the geologic rate [*Niemi and Hall*, 1992]. *Murray et al.*, [2014] estimated the deep slip rates on the northern San Andreas fault, Maacama fault and Bartlett Springs fault to be 21.5 ± 0.5 , 13.1 ± 0.8 , and 7.5 ± 0.7 mm/yr below 16 km, 9 km, and 13 km, respectively, using an expanded campaign GPS network spanning a latitude range between 39° and 40° . Alignment arrays (AA) and GPS suggest that the

northern San Andreas fault is fully locked and the other major faults are partially creeping at variable rates [Galehouse and Lienkaemper, 2003; Lienkaemper et al., 2014; Murray et al., 2014]. However, the limited spatial coverage of the ground-based geodetic data does not allow a complete recording of the near-field interseismic deformation associated with these faults and therefore prohibits a more refined assessment of their earthquake potential.

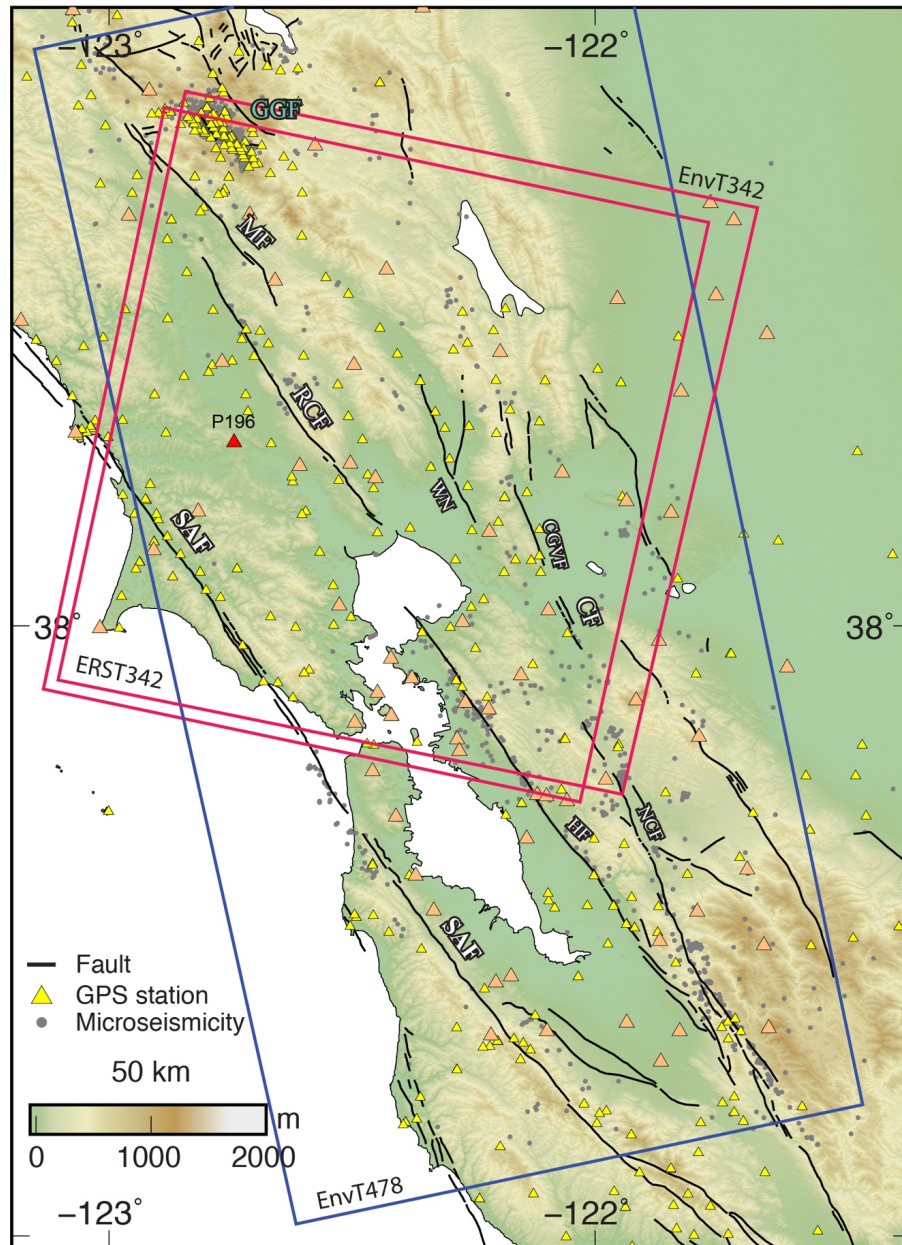


Figure 1. Map showing the datasets used in the study. Red and blue rectangles outline the existing InSAR scenes with tracks and satellite noted. The triangles indicate the location of continuous GPS sites (pink) from the PBO and BARD GPS networks and North Bay campaign sites (yellow). The reference GPS station P196 is highlighted in red. Active faults in the studied area shown in black lines: SAF, San Andreas fault; RCF, Rogers Creek fault; MF, Maacama fault; WN, West Napa fault; CGVF: Concord-Green Valley fault; CF, Concord fault; HF, Hayward fault; NCF, Northern Calaveras fault; GGF, Geysers geothermal field.

Interferometric Synthetic Aperture Radar (InSAR) has been widely used to constrain the locations of actively creeping faults in areas with limited ground access [Ryder and Bürgmann, 2008; Jolivet *et al.*, 2012; Metzger and Jónsson, 2014;]. It has provided important information on the spatio-temporal distribution of shallow aseismic fault slip [Çakir *et al.*, 2005; Fattahi and Amelung, 2016]. The combination of InSAR and GPS data has led to refined estimates of the amplitude of elastic strain accumulation on seismogenic faults and their locking depths with both a high spatial and temporal coverage [Wright *et al.*, 2001; Tong *et al.*, 2013]. Where large data sets are available InSAR has shown its ability to characterize both the long- and short-wavelength deformation to a very high accuracy, independent of GPS data [e.g., Chaussard *et al.*, 2015a]. A 30-image ERS satellite-based Permanent Scatterer InSAR (PS-InSAR) study spanning the time interval 1992-2001 suggests that the Rodgers Creek fault is undergoing as much as 7.5 ± 2.6 mm/yr of shallow creep above a depth of ~ 6 km [Funning *et al.*, 2007]. Combining Envisat data from both ascending and descending orbits, Jin and Funning [2017] found evidence for surface creep along a 20-km-long segment of the Rodgers Creek fault with rates between 1.9 and 6.7 mm/yr.

In this work, we expand previous studies by using a more complete InSAR data set covering the major faults in both ascending and descending orbits and spanning a ~ 20 -year time window between 1992 and 2010. We align the InSAR data to GPS velocities and deconvolve the InSAR mean velocities into horizontal and vertical components. We combine our new results from the North Bay with InSAR and updated GPS data from the central Bay Area [Chaussard *et al.*, 2015b]. We invert for the deep strike-slip rates on major faults in the greater Bay Area and use a forward model to simulate and remove the long wavelength signal from the fault horizontal mean velocity field. The remaining short-wavelength deformation shows shallow creep occurs along the Rodgers Creek and Concord faults, however, the data are not of high enough quality to allow for inversion of meaningful distributed creep models. We also observe significant and localized nontectonic surface processes in the North Bay.

2. Data and methods

2.1. InSAR data processing and time series analysis

In this study, data from three different satellites; i.e. ERS-1/2 and Envisat with a total of 88 SAR images, are used to resolve the 1992-2010 interseismic deformation in the North Bay. These data from two tracks (descending track 342 and ascending track 478) were obtained from the European Space Agency (ESA) through the Western North American interferometric synthetic aperture radar consortium (WInSAR) archive (Fig.1). After the concatenation of adjacent frame datasets, 274 interferograms were generated (Fig. S1, Table S1). In the interferometric chain, the 1 arc/sec (~ 30 m) Shuttle Radar Topography Mission digital elevation model [Farr *et al.*, 2007] is utilized to simulate and eliminate the topographic phase contribution with the GAMMA software. To increase the signal-to-noise ratio, the interferograms are multi-looked to around 100 square meters per pixel. We use the amplitude dispersive index of 0.6 (Ferretti *et al.*, 2001) to identify the candidate stable points. These selected points are spatially networked with arcs (e.g., triangular network or fully connected network) with each arc representing the double phase difference between two points. We unwrap the arcs temporally following the temporarily coherent point method presented by Pepe *et al.*, [2006] and Fornaro *et al.*, [2011]. The advantage of this unwrapping method is that it considers the phase triangularity algorithm in the SAR temporal/perpendicular baseline domain [Rocca, 2007; Monti Guarnieri *et al.*, 2008; Ferretti *et al.*, 2011]. We estimate the phase interval vector $\Delta\phi_i^{arc}$ on each arc using the least-squares inversion method. The detailed estimation of the double phase difference on the i -th arc is shown

as follows:

$$\underbrace{\mathbf{A}}_{M \times (N-1)} * \underbrace{\Delta \boldsymbol{\varphi}_i^{\text{arc}}}_{(N-1) \times 1} + \mathbf{e}_i = \underbrace{\Delta \Phi_i^{\text{arc}}}_{M \times 1} \quad (1)$$

$$\mathbf{A} = \begin{bmatrix} 1 & 1 & 0 & 0 & \dots \\ 0 & 1 & 1 & 1 & \dots \\ \dots & \dots & \dots & \dots & \dots \\ \dots & \dots & \dots & \dots & \dots \end{bmatrix}$$

$$\Delta \boldsymbol{\varphi}_i^{\text{arc}}(\boldsymbol{\theta}) = (\boldsymbol{\theta}_1 \ \boldsymbol{\theta}_2 \ \dots \ \boldsymbol{\theta}_{N-1})^T$$

Where \mathbf{A} represents the matrix with the dimensions of M by $N-1$ (M is the number of interferograms, N is the number of SAR images). More specifically, if the m -th interferogram covers n consequent time intervals, then the corner (m, n) of \mathbf{A} is equal to one and contains zeros elsewhere. The \mathbf{e}_i represents the estimated data errors. $\Delta \boldsymbol{\varphi}_i^{\text{arc}}$ is the $N-1$ by 1 matrix collecting the phase interval vector on the arc, $\boldsymbol{\theta}_i$ is the double difference phase on the arc, $\Delta \Phi_i^{\text{arc}}$ represents the double phase difference value on the arc.

Because multi-looked interferograms produce phase inconsistencies in the temporal/perpendicular baseline domain [De Zan, F. et al., 2015], we iteratively estimate the phase vector via Equation (1) and use the standard deviation of the residual (i.e., $\sigma_{\text{residual}} = 0.2$ rad) to exclude noisy arcs and weight the calculation in Equation (1) [Zhang et al., 2011]. Before the integration in the spatial domain, we detect the closure triangles with the remaining arcs and ensure the residual phase of closure triangularity is close to zero [Hanssen, 2001; Rocca, 2007; Agram et al., 2015]. The arcs and isolated points that have large phase variations or phase ambiguities are removed [Pepe et al., 2006]. Then, the standard deviation of the residual (i.e., σ_{residual}) can reasonably be used to set the weights associated with the single arcs (see (2) \mathbf{W}_p). Using Equation (2), the spatial integration for spatial phase unwrapping is executed to get unwrapped phase on the points, which is related to a reference point near a GPS station, which is shown as follows:

$$\left(\underbrace{\mathbf{B}^T}_{Q \times P} \underbrace{\mathbf{W}_p}_{Q \times Q} \underbrace{\mathbf{B}}_{Q \times P} \right) \underbrace{\boldsymbol{\Phi}^{\text{point}}}_{P \times N-1} = \underbrace{\mathbf{B}^T}_{Q \times P} \underbrace{\mathbf{W}_p}_{Q \times Q} \underbrace{\Delta \boldsymbol{\varphi}^{\text{arc}}}_{Q \times N-1} \quad (2)$$

$$\mathbf{B} = \begin{bmatrix} 1 & -1 & 0 & 0 & \dots \\ 0 & 1 & 0 & -1 & \dots \\ \dots & \dots & \dots & \dots & \dots \\ \dots & \dots & \dots & \dots & \dots \end{bmatrix}$$

$$\mathbf{W}_p = \begin{cases} \frac{1}{(1 + \sigma_{\text{residual}})}, & \sigma_{\text{residual}} < \delta \\ 0, & \sigma_{\text{residual}} \geq \delta \end{cases}$$

Where \mathbf{B} is a Q by P matrix (Q is the number of arcs and P is the number of points) that presents the network design matrix. $\Delta \boldsymbol{\varphi}$ collects all the phase vectors on the arc with Q by $N-1$ dimension. \mathbf{W}_p is a Q by Q diagonal weighting matrix and δ is an experimental threshold value. $\boldsymbol{\Phi}^{\text{point}}$ is a P

by N-1 matrix containing the phase history vector on the points.

When the unwrapped phase history vectors of the points are available, the deformation and topographic residual can be parameterized and estimated. Noise from atmospheric artifacts is reduced using a Principal Component Analysis-based inversion method (*Lin et al.*, 2010). In addition, the Local Oscillator drift (LOD) seen in the Envisat interferograms is corrected using the empirical model proposed by *Marinkovic and Larsen*, [2013]. The remaining data noise mainly consists of small orbital errors and atmospheric artifacts, which we mitigate with the help of all available 3D GPS velocities. We identify the noisy part from the InSAR long wavelength deformation field, and use the GPS to constrain a quadratic function.

After we remove the estimated ramps from the LOS velocity maps on the different tracks; i.e., ascending and descending orbits, we assume that the updated LOS velocity is a combination of the east-west horizontal displacement rate (u_e) and vertical motion (u_v) by ignoring the north-south component. We validate the decomposed velocity fields by comparing them with GPS east-west and vertical velocities and observe agreement with an RMS value of ~ 3 mm/yr and ~ 9 mm/yr, respectively (Fig. S2). Note that the RMS decreases to 2 mm/yr and 4 mm/yr if the Geysers region is excluded. This is likely due to deformation rates associated with the geothermal extraction and injection activity at the Geysers varying strongly in time [*Mossop and Segall*, 1997; *Vasco et al.*, 2013; *Floyd and Funning*, 2013].

2.2. GPS data processing

For comparison with the InSAR-derived velocity field, we compile multiple sources of GPS velocities into a single GPS velocity field. This reference velocity field includes the Bay Area Velocity Unification model (BAVU4) velocity field, derived from campaign GPS measurements in the Bay Area and processed with the GAMIT/GLOBK software [*Herring et al.*, 2010a]. This represents an update of the GPS velocities presented by *d'Alessio et al.* [2005] with more recently collected data in the central Bay Area. Velocities from the Plate Boundary Observatory and Bay Area Regional Deformation network are combined with BAVU4 using the GLOBK software package [*Herring et al.*, 2010b]. In addition, velocity fields from the USGS campaign and continuous networks [*Murray and Svarc*, 2017] and from *Floyd et al.* [2016] are also combined into the reference field. For the velocity field combinations, we used a 6-parameter Helmert transformation with 3 rotation and 3 translation parameters to minimize the misfit between the stations common to multiple networks. We exclude 144 out of 1592 stations with formal uncertainties of more than 3 mm/yr from the Helmert transformation and combined velocity field. The resulting velocity field represents a dense collection of Bay Area campaign and continuous GPS velocities with respect to a common reference. The RMS misfit values during the adjustment of velocity fields by Helmert transformation ranged from 0.7 mm/yr to 1.7 mm/yr for the common stations.

2.3. Repeating earthquakes

While geodetic data provide information on fault slip at depth through the filter of the Earth's crust, characteristically repeating earthquakes (CREs) provide direct measurements of creep at their precise location at depth on an actively creeping fault plane [*Nadeau and McEvilly*, 1999; *Nadeau and McEvilly*, 2004; *Chaussard et al.*, 2015b]. Considering the uncertainty of the method, CREs may represent creep slip events such that creep rates derived from CRE recurrence times would represent minimum bounds [*Beeler et al.*, 2001]. CRE sequences are events occurring in essentially identical locations, with similar magnitudes, and with high waveform correlation

coefficients. We searched for the existence of CREs on the North Bay faults to identify creeping fault sections. We used the Double-Difference Real-Time catalog and follow the method of *Turner et al.*, [2013] relying on events from the Northern California Earthquake Data Center (NCEDC) detected by the Northern California Seismic System (NCSS). We have developed an automated method of waveform cross-correlation analysis in the frequency domain using a ~ 5 second data window starting ~ 0.5 sec before the P-wave phase arrival performed on pairs of events with $M > 1.2$ and hypocentral separations ≤ 10 km. We consider as potential CREs event pairs with maximum cross-correlation values > 0.6 , focusing on event identification rather than on the full characterization of CRE sequences. We find four repeating sequences on the Rodgers Creek fault, two of which are located to the south of Santa Rosa at ~ 4.5 km depth with a magnitude < 3 , the other two found north of Santa Rosa at depths of 6.5 km and 9.1 km with a magnitude of ~ 2 , respectively. Two CREs of magnitudes < 2 are found on the Concord fault at a depth of ~ 6 km. There are two sequences near the West Napa fault with a magnitude of 1.8 at depths of 6.5 km and 7.3 km, respectively. Three CREs with magnitudes ranging between 1.8 and 2.5 are aligned with the Concord Green Valley fault zone at depths increasing from 2.7 km in south to 8 km in north. In contrast, a substantially larger number of CREs are identified on the partially coupled Hayward and Calaveras faults that creep at rates of up to 14 mm/yr [*Chaussard et al.*, 2015b].

3. Surface creep in the North Bay

The descending ERS-1/2 data comprise SAR images obtained between April 1992 and July 2002 (Fig. 2 and Table S1) and show surface creep along the Concord fault and sections of the Rodgers Creek fault. The creeping signal generated by the Hayward fault is also clear. It is difficult to resolve whether surface creep occurs on other major faults in the North Bay from this single viewing geometry. The descending Envisat data (Fig. 3), covering a later and shorter time period (2006–2010), confirms the observations of the ERS-1/2 data. The viewing geometry of the ascending Envisat mean velocity field, however, is less favorably oriented to resolve horizontal motion along the San Andreas fault system (Fig. 4). Therefore, the ground deformation seen from the ascending data more likely reflects vertical motions.

Through the decomposition of the ascending and descending InSAR mean velocity fields, we resolve a detailed spatial coverage of the interseismic InSAR mean horizontal velocity and vertical motions in the North Bay where the descending and ascending images overlap. The horizontal deformation includes two main components: the long-wavelength deformation resulting from interseismic elastic strain accumulation along locked faults in the Bay Area (Fig. 5a) and the short-wavelength deformation seen near the Rodgers Creek, Concord and Hayward-Calaveras faults, representing shallow creep (Fig. 6). We adopt the Bay Area fault geometry of *Funning et al.*, [2007] and combine our data with the published central Bay Area data [*Chaussard et al.*, 2015b] to cover major faults in the greater Bay Area. To model the data, we use the rectangular dislocation model [*Okada*, 1985] assuming a homogeneous and isotropic elastic half-space. We jointly invert both the combined GPS east mean-velocity field and the combined InSAR east mean velocity field to estimate the deep slip rates on major locked faults in the greater Bay Area (Fig. 5). The locking depths are adopted from the published result [*Funning et al.*, 2007]. The inversion is done using a constrained linear least-squares method, in which the slip rates of the faults that are located outside the study area are fixed. The combined InSAR horizontal mean velocity field and GPS data are equally weighted in the modeling. The simulated long-wavelength deformation (Fig. 5b) agrees well with the data with a root mean square (RMS) misfit of ~ 2.6 mm/yr. We find that the re-estimated deep slip rates are generally consistent with previous estimates [*Freyemueller et al.*, 1999,

Prescott et al., 2001, Bürgmann et al., 2006, Funning et al., 2007; Murray et al., 2014; Field et al., 2015]. The jointly modeled long-term slip rates are 19.2 ± 0.8 mm/yr on the San Andreas Peninsula segment, $\sim 11.6 \pm 0.5$ mm/yr on the Rodgers Creek fault and $\sim 11.5 \pm 0.6$ on the Green Valley fault (Table 1).

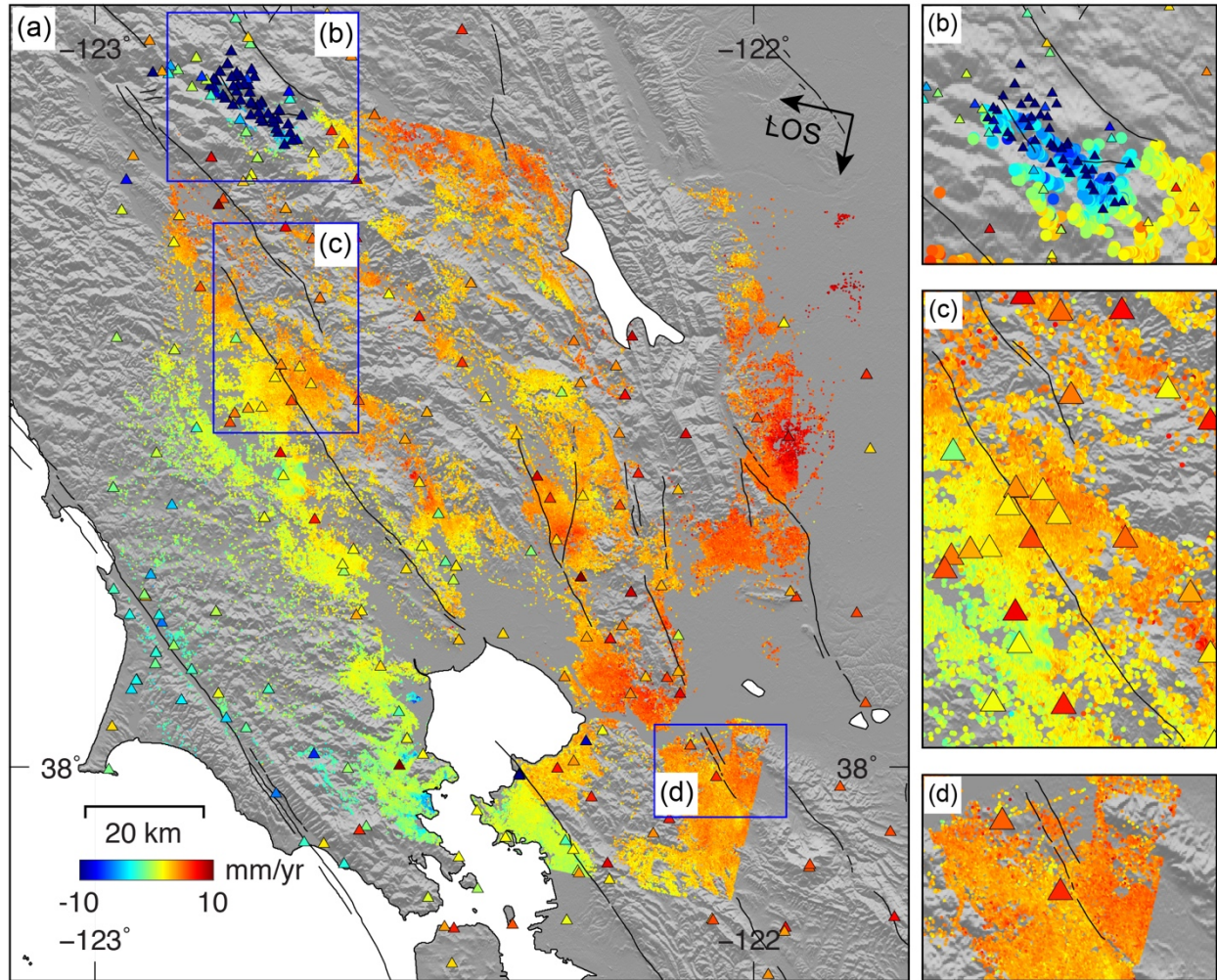


Figure 2. (a) InSAR mean LOS velocity field and GPS horizontal velocities projected into LOS (color-coded triangles) covering the major faults in the North Bay generated using ERS-1/2 SAR data (between April 1992 and July 2002) from the descending orbit. The solid black lines represent the mapped fault traces. Negative LOS values indicate the ground moves away from the satellite. (b-d) Enlarged view of the Geysers geothermal region, the RCF and the CF. Note that the color scale is the same in different subpanels.

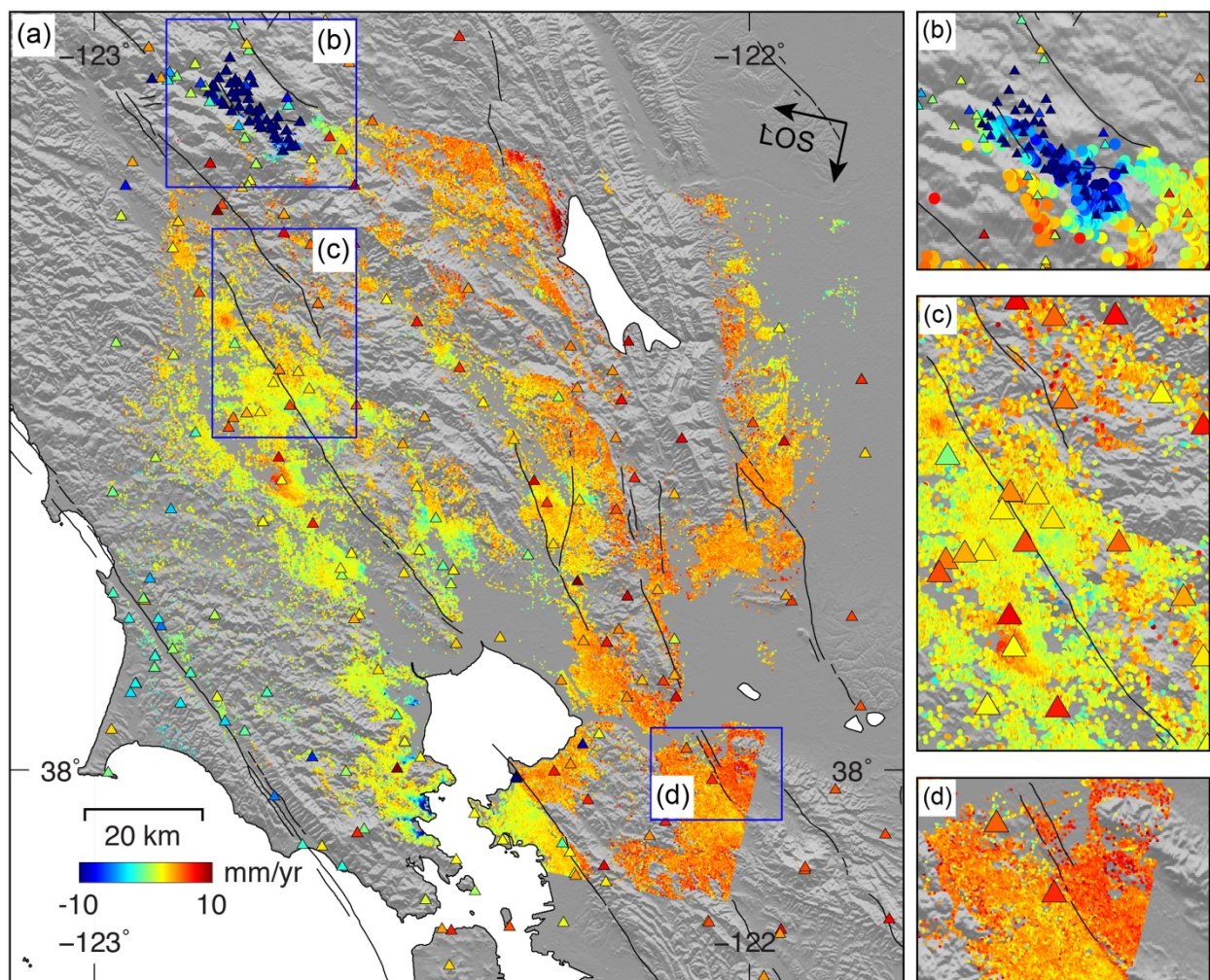


Figure 3. same as Fig. 2, but for the descending Envisat SAR data spanning May 2006 through October 2010.

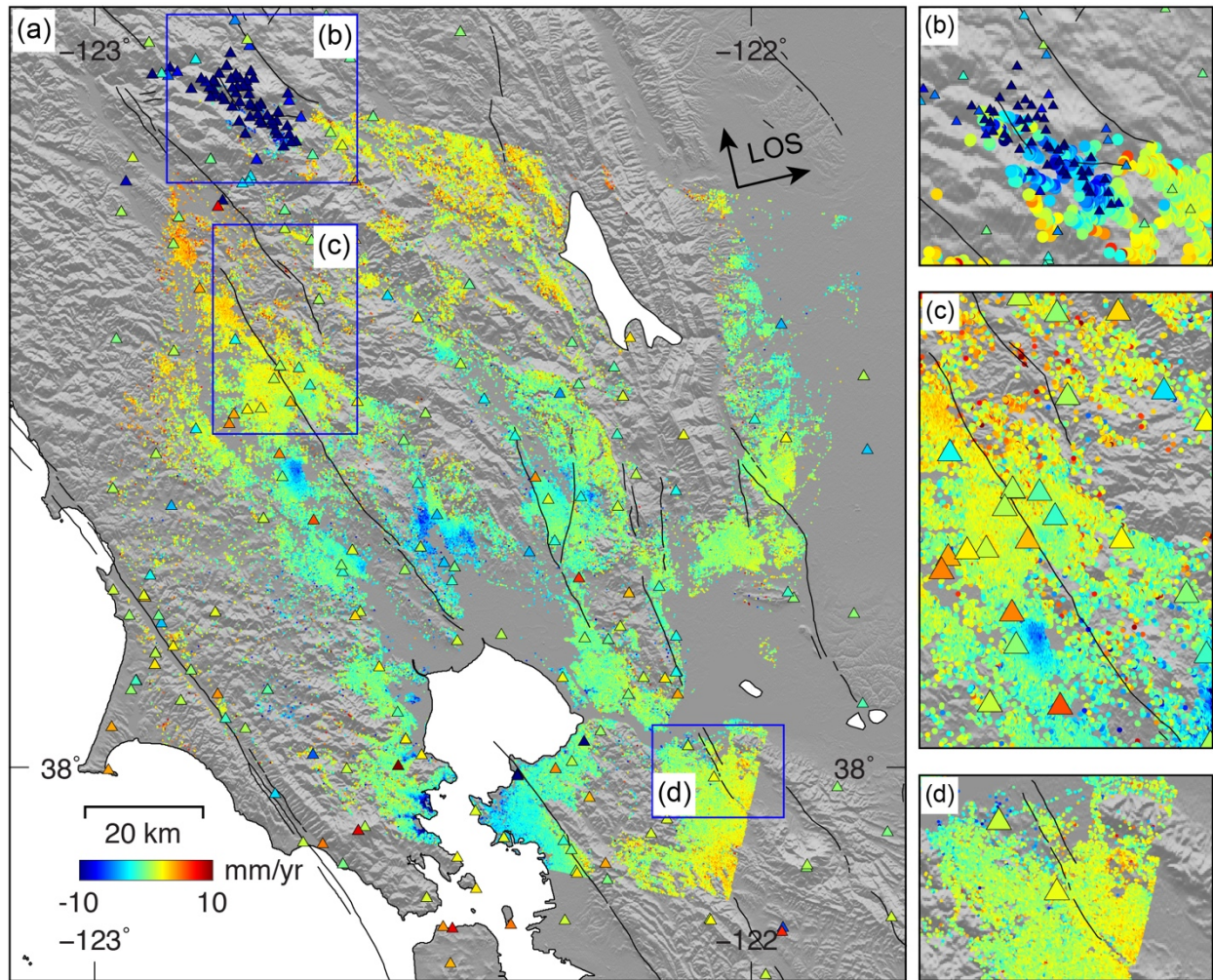


Figure 4. same as Fig. 2, but for the ascending Envisat SAR data spanning October 2006 through October 2010.

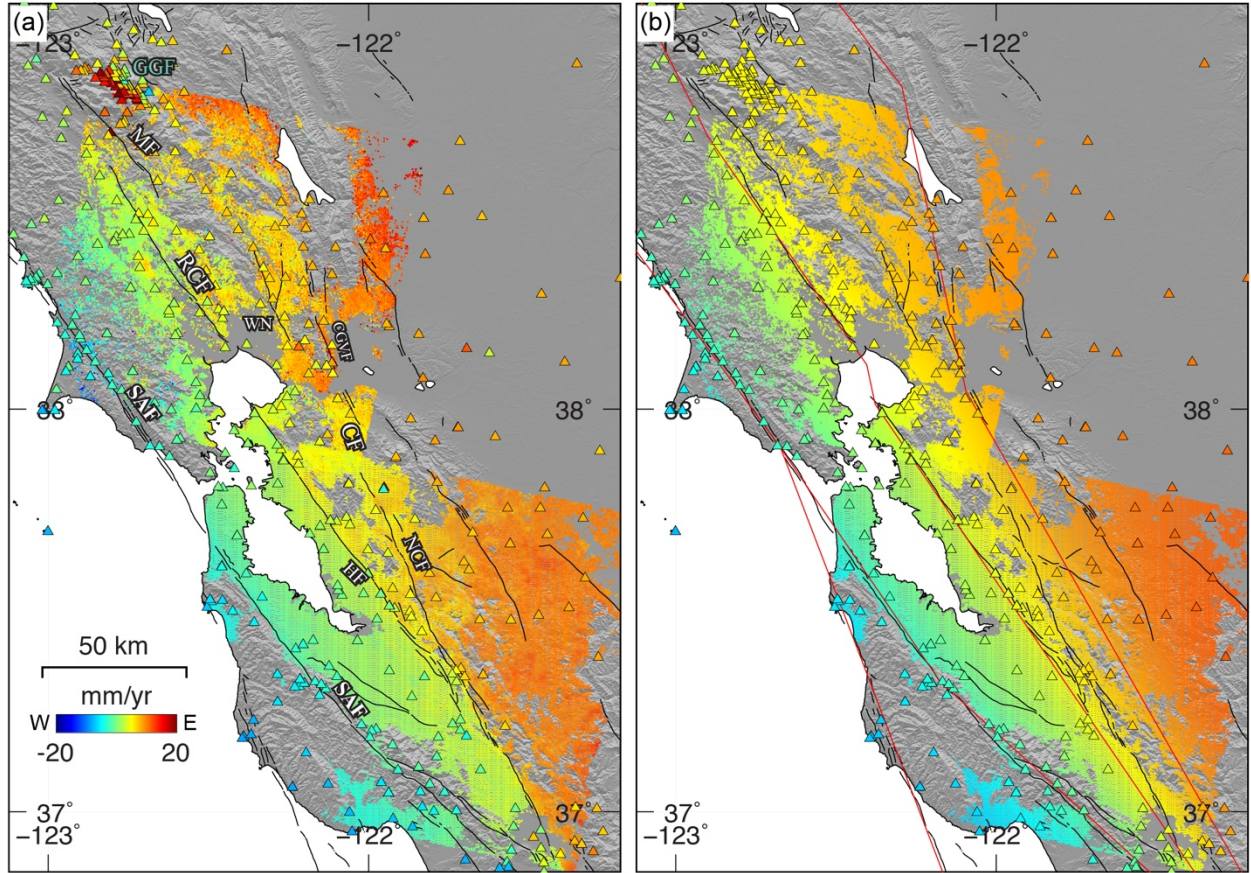


Figure 5. (a) East component of InSAR and GPS mean velocities (color-coded) covering the North Bay (this analysis) and the central San Francisco Bay Area (from Chaussard et al., 2015). Colored triangles in (a) show GPS measured east-component velocities of campaign measurements and continuous PBO and BARD stations in the area. Positive values indicate movement to the east in (a). (b) East velocities predicted from the deep dislocation model; the surface trace of the modeled fault geometry is based on Funning et al. (2007). The black lines show the surface projection of the mapped faults. The red lines indicate the surface projection of the vertical dislocations extending downward from 12 km.

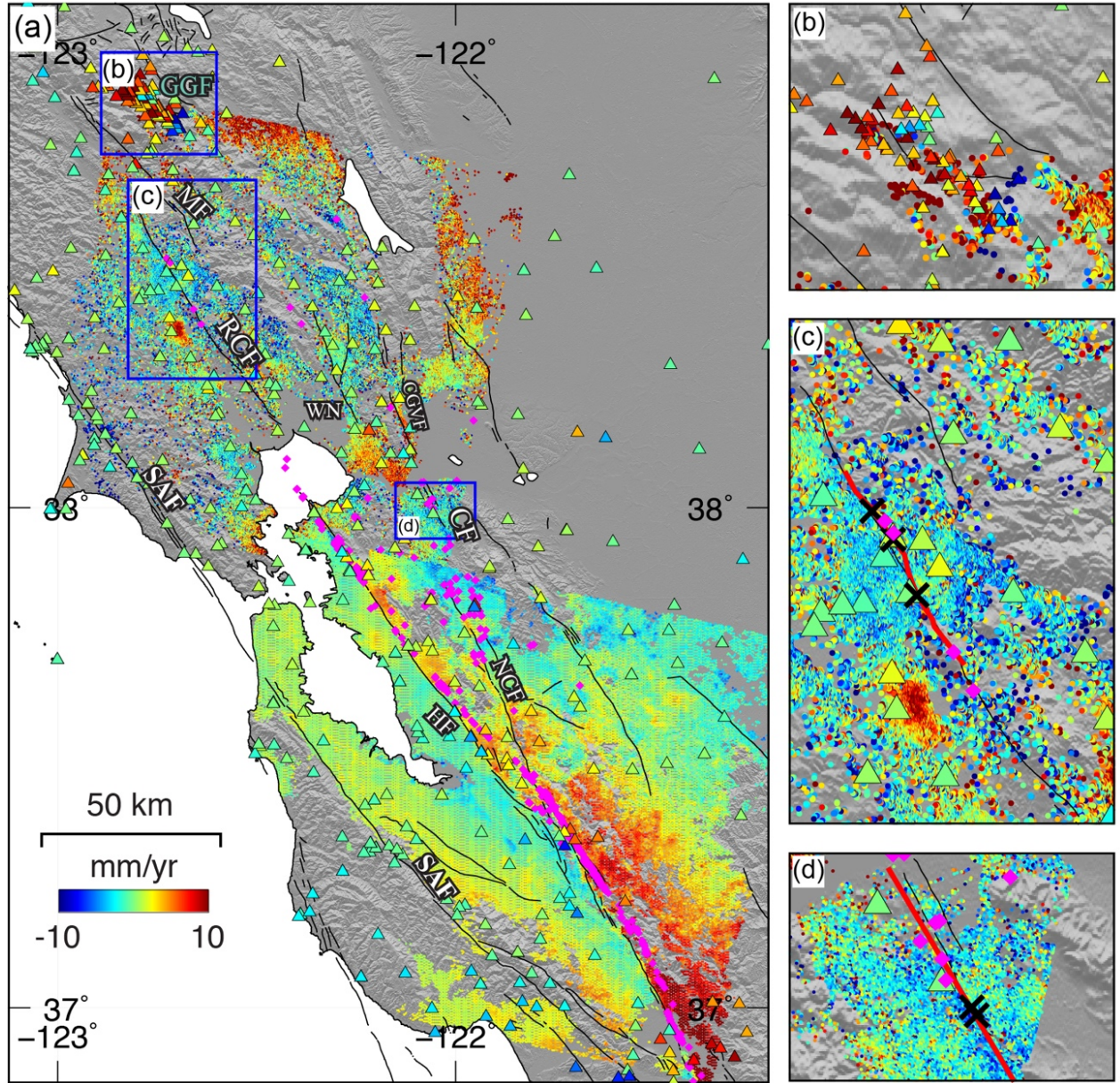


Figure 6. (a) SAF fault-system-parallel (N32°W) residual velocity field of the greater Bay Area obtained by subtracting the long-wavelength deformation from the deep dislocation model shown in Fig. 5b. The magenta dots represent the location of repeating earthquakes. (b) Enlarged view of the Geysers geothermal region showing significant horizontal motion. (c) Enlarged view of the RCF – MF. Black crosses indicate the locations of alignment arrays; red lines indicate the locations of profiles shown in Fig. 7. (d) Enlarged view of the concord fault.

The short-wavelength deformation is obtained by subtracting the modeled long-wavelength rate (Fig. 5b) from the observation (Fig. 5a). According to *d'Alessio et al.* (2005), the total relative motion accommodated by Bay Area faults is 37.9 ± 0.6 mm/yr oriented at N30.4°W in the central North Bay and at N34.2°W in the central South Bay. We project the short-wavelength horizontal velocity field into fault-parallel rates in the direction of N32°W to reflect the actual creep rates.

Shallow fault creep is seen along the Hayward and Calaveras faults in the East San Francisco Bay Area [Chaussard *et al.*, 2015b], while the creep signal is less obvious in the North Bay. We calculate the creep rates based on the difference in fault-parallel velocity binned in boxes on opposite sides of the fault (Fig. S3-S4). Plotting along-fault profiles on our InSAR horizontal velocity map (Fig. 7a), we estimate the average creep rate of the Rodgers Creek fault is about 2 mm/yr along much of its trace, consistent with the AA data, although the AA data seem to suggest that the along-fault creep rates decrease from north to south (Fig. 7a and Fig. S5). Our estimated slip rate of 2 mm/yr is slightly higher than the lower bound (0.4 mm/yr) of a recent estimated value by Jin and Funning, [2017] and is much lower than the 6 ± 0.6 mm/yr rate that was estimated from seven years of ERS-1/2 data [Funning *et al.*, 2007]. Limited near-fault coverage southeast of Santa Rosa prohibits identifying evidence of shallow creep, similar to previous studies [Funning *et al.*, 2007; Jin and Funning, 2017]. Another interseismic creep signal ranging between 2 mm/yr and 4 mm/yr is identified along the Concord fault (Fig. 7b). These values agree well with the two AA estimates. The InSAR data show that the along-fault creep rate on the northern and southern sections of the Concord fault is likely lower than along its central part (Fig. 7b). Similar to previous findings [Chaussard *et al.*, 2015a], we observe obvious shallow creep signals along the southern section of the Hayward fault. Nontectonic signals are mostly seen to the northeast of the image, possibly due to a horizontal component associated with land subsidence along the margins of the Central Valley.

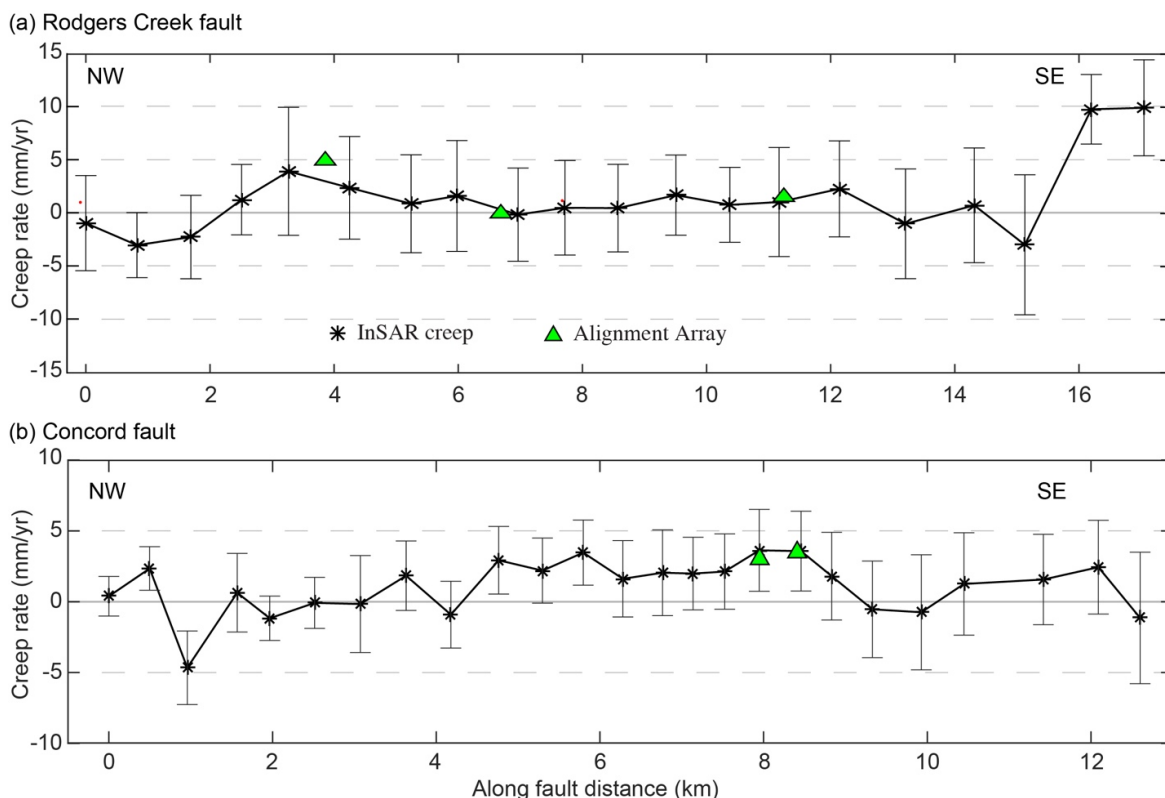


Figure 7. Along fault variations of creep rates for (a) RCF and (b) CF. Black cross represents the calculated InSAR creep rate with 68% (1σ) uncertainties. Green triangles show local creep-rate estimates from alignment arrays (Lienkaemper *et al.*, 2014). The location of the profiles is shown in Fig. 6c and d.

4. Vertical deformation in the North Bay

The InSAR vertical displacement field shows significant localized vertical motions due to geothermal, hydrological and sediment compaction processes (Fig. 8). The maximum vertical land subsidence rate of ~ 17 mm/yr is observed in the Geysers Geothermal Field between 1992 and 2010, which is mainly associated with geothermal production (Fig. 8b). This value is lower than previous subsidence estimates of up to 48 mm/yr from 1994 – 1996 campaign GPS observations [Mosso and Segall, 1999], an average of 20 mm/yr observed from campaign GPS measurements from 1994 and 2011 made by Floyd and Funning, [2013], and an estimate of up to 50 mm/yr in LOS from 1992 - 1999 ERS 1/2 InSAR data [Vasco et al., 2013], suggesting strong temporal variations in subsidence rates due to changing production and water injection rates. Significant localized horizontal deformation is also observed near the Geysers and appears bounded by the Collayomi fault to the east and the Maacama fault to the west (Fig. 8). Other areas of significant vertical deformation are mostly localized and associated with human activities in three regions in the North Bay (Fig. 8). Localized subsidence signals of up to ~ 7 mm/yr near Rohnert Park (Fig. 8c) and up to ~ 6 mm/yr in the Sonoma Valley (Fig. 8d) are related to groundwater withdrawal in local aquifers [e.g., Funning et al., 2007; McPhee et al., 2007; Jin and Funning, 2017]. Differences in vertical rates in these areas between the 1992-2002 and 2006-2010 observation periods (Fig. S6) are likely due to variable climate and/or groundwater withdrawal [e.g., Chaussard et al., 2014]. Many regions along the western Bay margin show significant localized subsidence signals of up to 10 mm/yr, likely due to consolidation of man-made fill and bay mud [e.g., Ferretti et al., 2004; Shirzaei and Bürgmann, 2018].

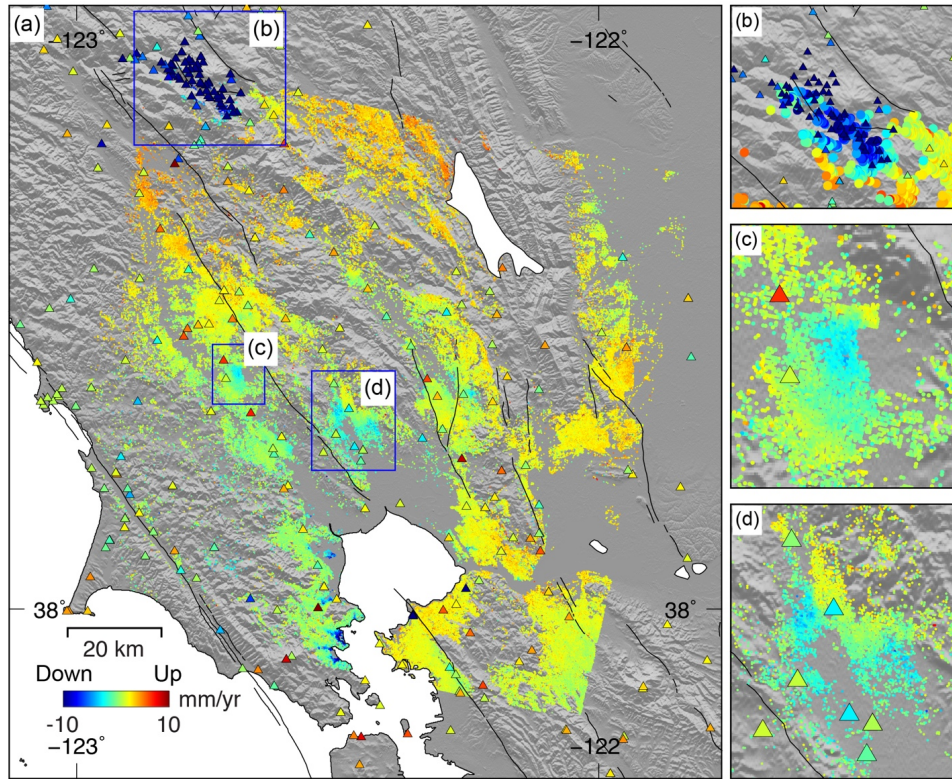


Figure 8. (a) InSAR and GPS vertical velocity field. Negative deformation rates indicate subsidence; Localized subsidence features are seen in (b) the Geysers geothermal region, (c) Rohnert Park, (d) the Sonoma basins.

5. Discussion

Paleoseismologic studies suggest that the Rodgers Creek fault is slipping at a rate of 6.4-10.4 mm/yr with a rupture recurrence interval of 131-370 yr south of Santa Rosa [Hecker *et al.*, 2005; Budding *et al.*, 2012]. Recent analyses of InSAR data suggest that the surface creeping rate of the Rodgers Creek fault is at lower rates ranging from 1.9 to 6.7 mm/yr north of Santa Rosa [Funning *et al.*, 2007; Jin and Funning, 2017]. Our InSAR mean velocity field and GPS data show that a shallow aseismic creep rate of ~ 2 mm/yr occurs in the city of Santa Rosa above a strong asperity that was inferred by Hecker *et al.*, [2016] from gravity and magnetic field anomalies. Because of vegetation in the regions north of Santa Rosa, the ability of InSAR to resolve creep on the fault decreases significantly. We therefore don't have quantitative estimates of how much of the estimated slip deficit is accommodated by aseismic creep, and we cannot provide evidences for presence or absence of creep along the northernmost section of the Rodgers Creek fault. However, the few identified CREs along the Rodgers Creek fault suggest that the creep rate increases from ~ 4 mm/yr south of Santa Rosa to ~ 6 mm/yr north of Santa Rosa.

Our results show that the predominantly right-lateral strike-slip Concord fault exhibits fault creep for much of its length. The rate increases from 2 mm/yr to 4 mm/yr from north to south. It is thought that the Concord fault connects with the Green Valley fault zone to the north, and the combined Concord-Green Valley fault zone has the capability to produce an event as large as M7 [Rowshandel *et al.*, 2006], which poses significant hazards to the nearly 1 million people in Contra Costa county, as well as to the rest of the Bay Area. Trenching of the Concord fault near Galindo Creek by Borchardt *et al.*, [1999] suggests slip rates from 3.4-5.4 mm/yr, where 3.4 ± 0.3 mm/yr was the best constrained number and 5.4 mm/yr was the maximum limit. These rates are all slower than the 6.8 ± 1.4 mm/yr determined geodetically from 1995-2005 GPS data [d'Alessio *et al.*, 2005]. The lower geologic rate is similar to the secular creep rates of 2.9-3.7 mm/yr as measured by two AAs on the central Concord fault [Lienkaemper *et al.*, 2014; McFarland *et al.*, 2016] and our InSAR results. This would suggest that creep is accommodating nearly all motion on the fault and that large earthquakes would not be generated. There is also a possibility of temporal change in strain accumulation through shallow fault creeping. However, if the current strain accumulation rate is more similar to the geodetic rate estimated by d'Alessio *et al.* [2005], then only half of the Concord fault's slip budget can be accounted for by creep. The estimated deep slip rate (15.9 mm/yr) of the Concord fault is nearly four times higher than the geological rate (4.3 mm/yr) [Field *et al.*, 2013]. We believe this high rate likely reflects the difficulty of obtaining a slip rate on this fault from geodetic data and the shallow slip deficit rate on this fault is likely to be small.

We do not see clear surface creeping signals on the West Napa fault and other major faults in our study area. These major faults lie near urban cities including Santa Rosa, Napa, Vallejo, and Concord posing significant seismic hazards to life and property. The slip behavior of the West Napa fault is poorly constrained with slip rates ranging from ~ 0 to 6 mm/yr [Field *et al.*, 2015]. Alignment array data collected over 18 year period for the West Napa fault indicate no surface creep [Galehouse and Lienkaemper, 2003], but this fault produced the M6 earthquake that hit Napa County on August 24, 2014, followed by a period of localized aseismic afterslip [Feng *et al.*, 2015; Floyd *et al.*, 2016]. We identified two CREs with a creep rate of 12 mm/yr and 7 mm/yr near the West Napa fault, which seem to indicate that fault creep may occur on this fault either at a rate unresolvable by our measurements or with variable rates. Similarly, no surface creep is observed geodetically for the Green Valley fault. However, alignment array data indicate greater creep rates on the Green Valley fault than on the Concord fault [Galehouse and Lienkaemper, 2003].

6. Conclusions

We show that time series analysis of two decades of InSAR data can be used to constrain rates of interseismic strain accumulation along major faults and resolve vertical motions in local regions in the North Bay. The decomposed InSAR horizontal mean velocity maps show evidence of shallow fault creep associated with the Rodgers Creek and Concord faults. The along-fault creep rate is ~ 2 mm/yr on the Rodgers Creek fault near the city of Santa Rosa and up to 4 mm/yr on the Concord fault, respectively. We do not observe obvious creeping signals on other major faults in the North Bay. The geodetic measurements also put constraints on the amount and patterns of vertical motion. In the Geysers geothermal region, the average land subsidence rate during the 1992-2010 period is about 10 mm/yr. In the Sonoma Valley and near Rohnert Park, vertical motions at rates of > 5 mm/yr are most likely related to changes in groundwater level. Although the archived ERS-1/2 and Envisat InSAR data help refine the crustal deformation field of the area and resolve smaller-scale deformation features, such as aseismic fault creep, land subsidence and geothermal deformation, the noise in the North Bay measurements still does not allow for using these data to invert for detailed coupling models on these faults, as was done for the Hayward – Calaveras faults [e.g., *Schmidt et al.*, 2005; *Shirzaei and Bürgmann*, 2013; *Chaussard et al.*, 2015b]. Continued acquisitions by the active Sentinel-1A/B satellites, which routinely collect data at 12-day intervals, and the L-band ALOS-2 satellite and the NASA-ISRO SAR mission should provide much improved data constraints within a few years.

Acknowledgments

The ERS and Envisat original data are copyrighted by the European Space Agency and were provided through the WInSAR archive. Waveform data, metadata and data products for this study were accessed through the Northern California Earthquake Data Center [NCEDC, 2014]. The GPS velocities were provided by USGS (doi:10.5066/F7NG4NRK), UNAVCO (doi: 10.7283/T5MW2F2D). The North Bay campaign GPS velocities can be obtained from Mike Floyd (<http://web.mit.edu/mfloyd/www/>). Several figures were prepared by using Generic Mapping Tools software. The research was supported by a U.S. Geological Survey National Earthquake Hazards Reduction Program (NEHRP) grant (G16AP00007), the Hong Kong Polytechnic University startup grant (1-ZE6R) and the Hong Kong Research Grants Council Early Career Scheme Fund (Project No. F-PP4B).

Appendix – Supplementary Figures

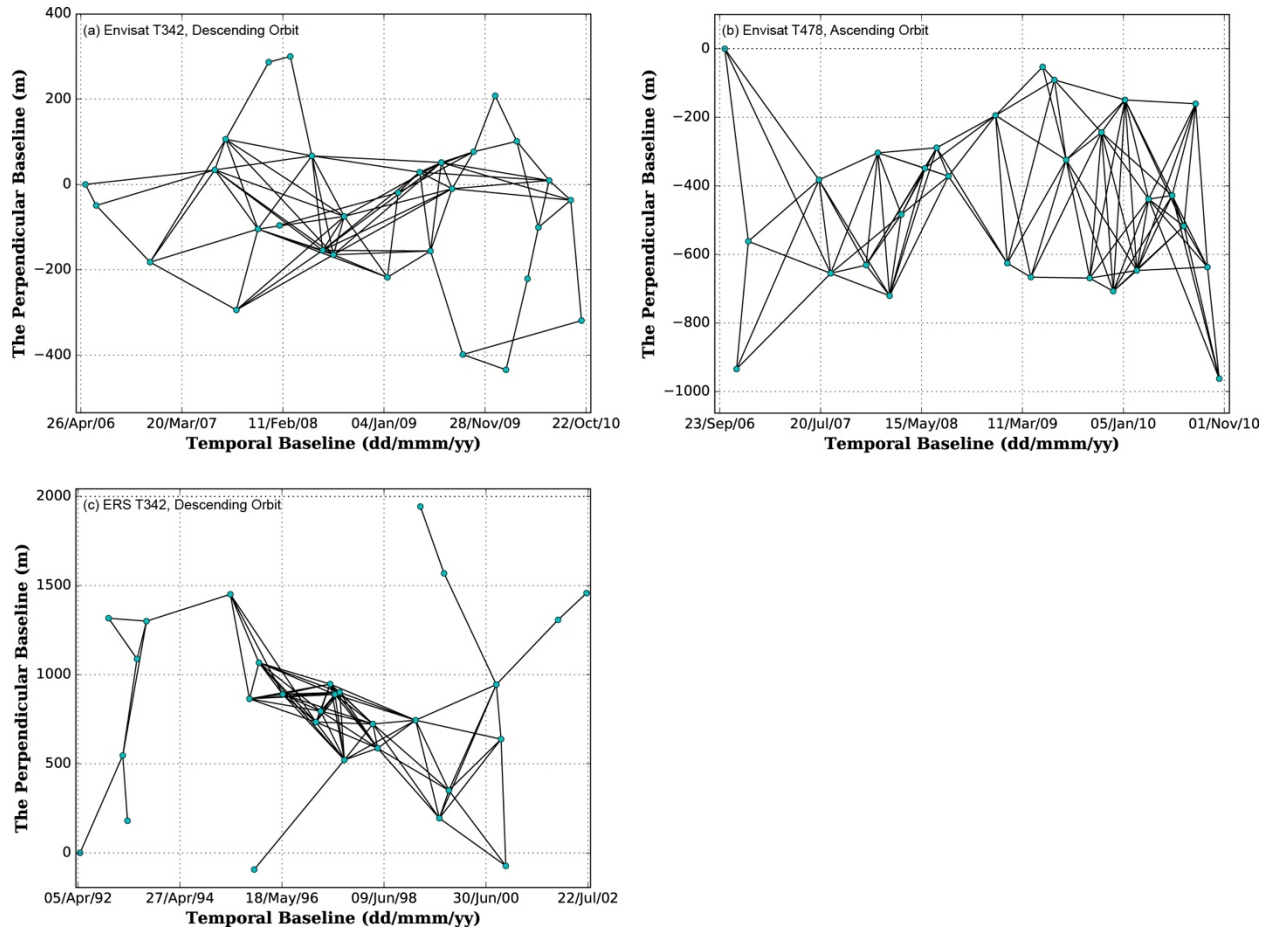


Figure S1. Orbit and temporal baselines of the interferometric pairs of (a) Envisat data on track 342, (b) Envisat data on track 478 and (c) ERS data on track 342. The SAR data processing and the time series calculations were carried out on a 64-bit PC with six Corei7-6800K processors. The overall operation time of our time series processing method requires ~6 hours for one data set.

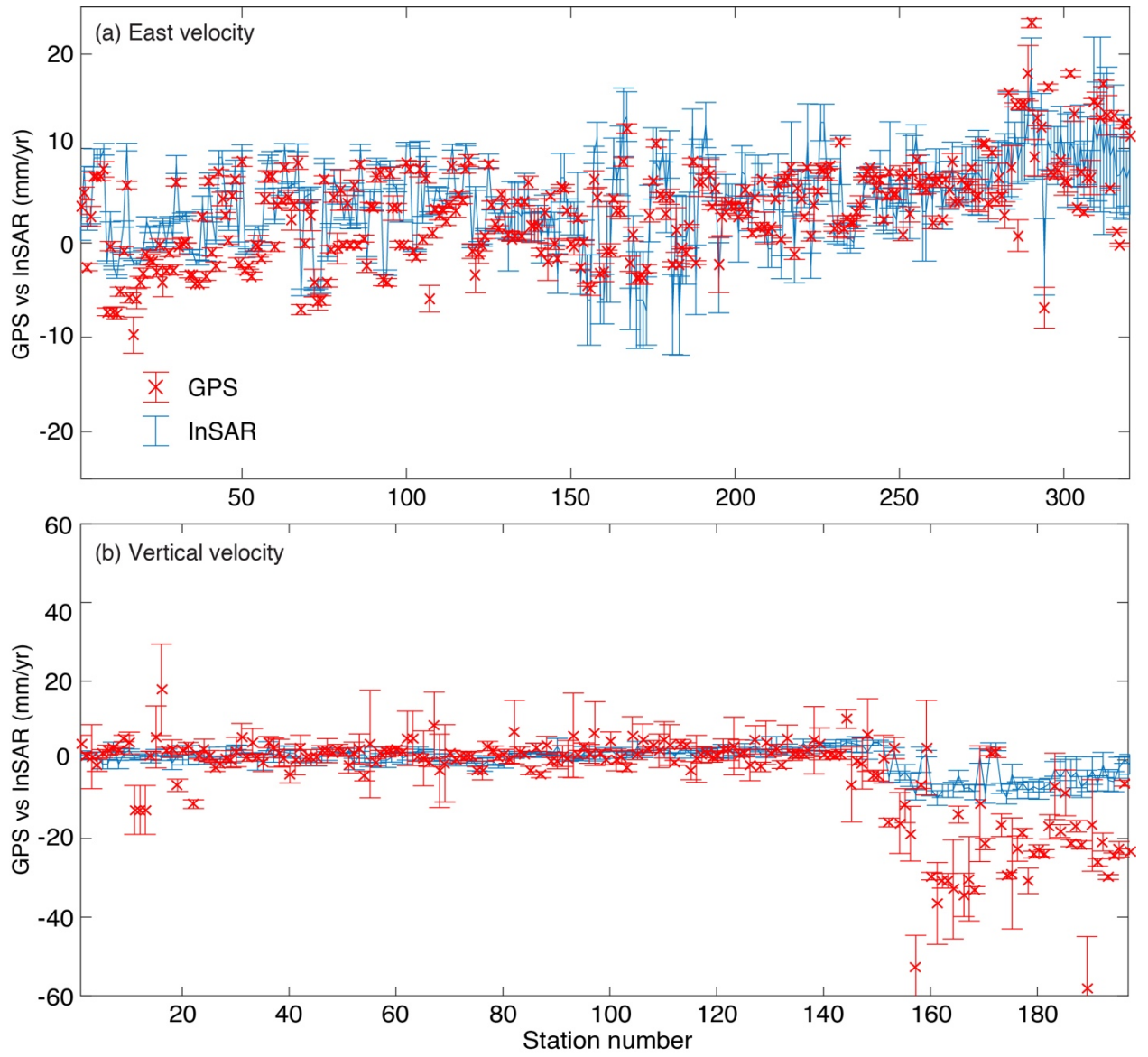


Figure S2. Comparison between GPS (red, with 1σ error bars) and InSAR-derived (a) east and (b) vertical mean velocities (mm/yr) at the locations of GPS sites ordered by increasing latitude.

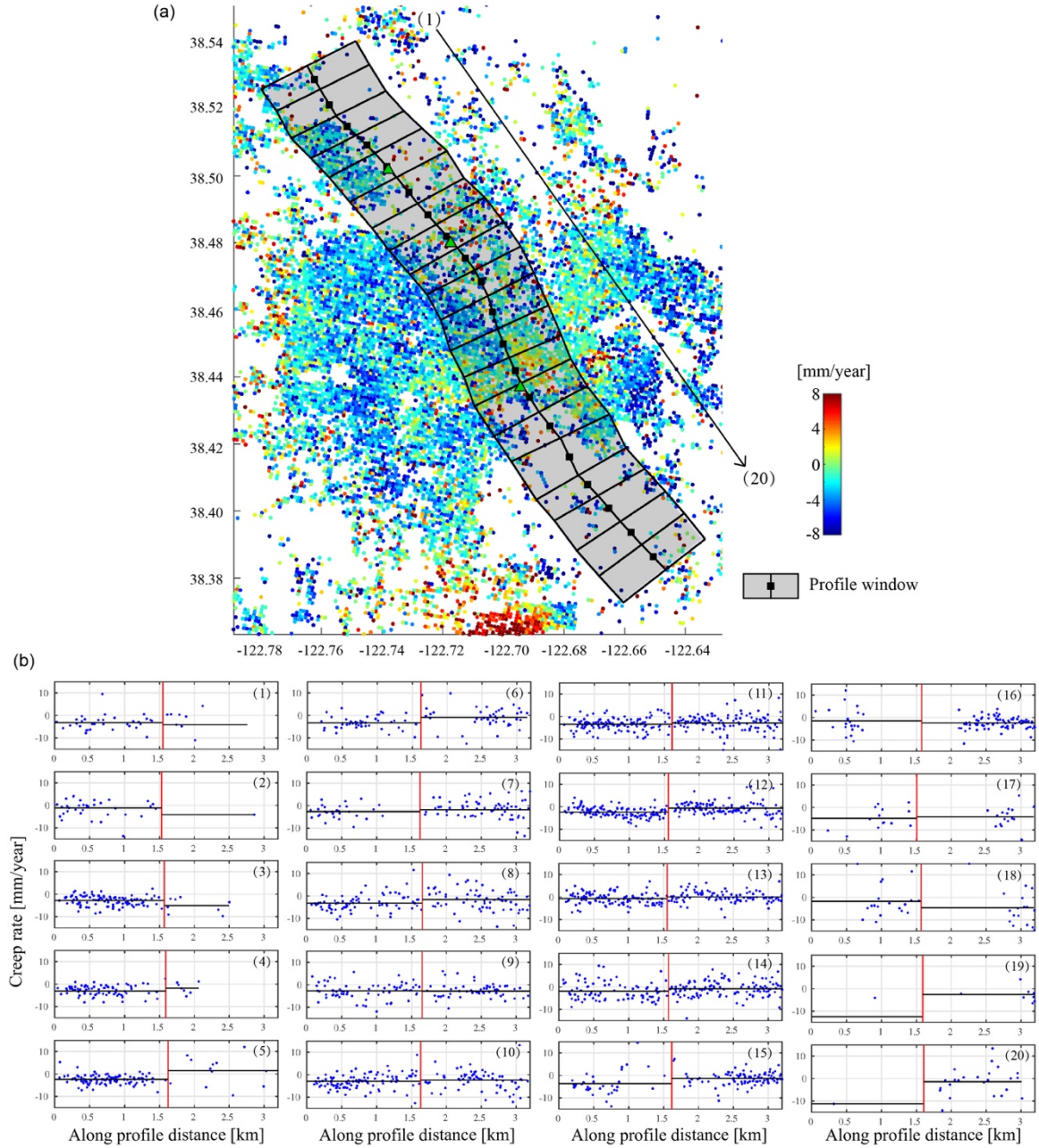


Figure S3. Regional surface velocity field along the Rodgers Creek fault. The creep rates are calculated based on the difference in fault-parallel velocity binned in the shaded boxes on opposite sides of the fault. The dimension of the selected boxes is 3.2×0.8 km. See Fig. 7a and Fig. S5 for along-fault profile of the estimated surface offsets.

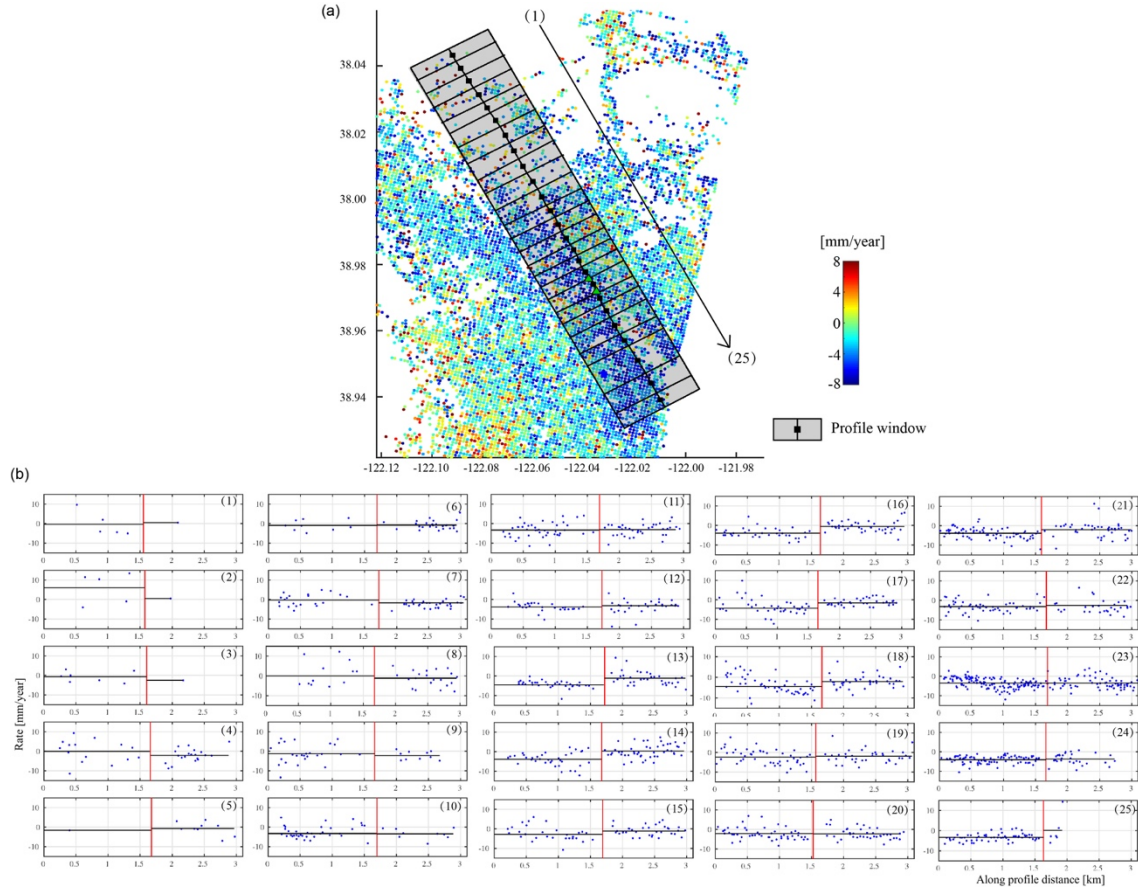


Figure S4. Same as Fig. S3, but for the regional surface velocity field along the Concord fault. The dimension of the selected boxes is 3.2×0.5 km. See Fig. 7b along-fault profile of the estimated surface offsets.

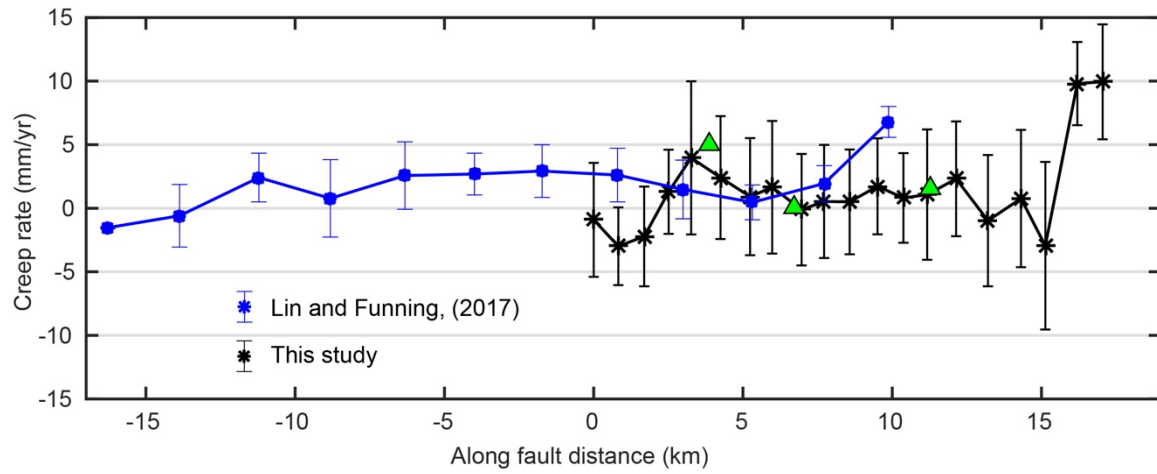


Figure S5. Same as Fig. 7, but also including the previously published creep rate variations with 2σ uncertainties shown in blue (Jin and Funning, 2017).

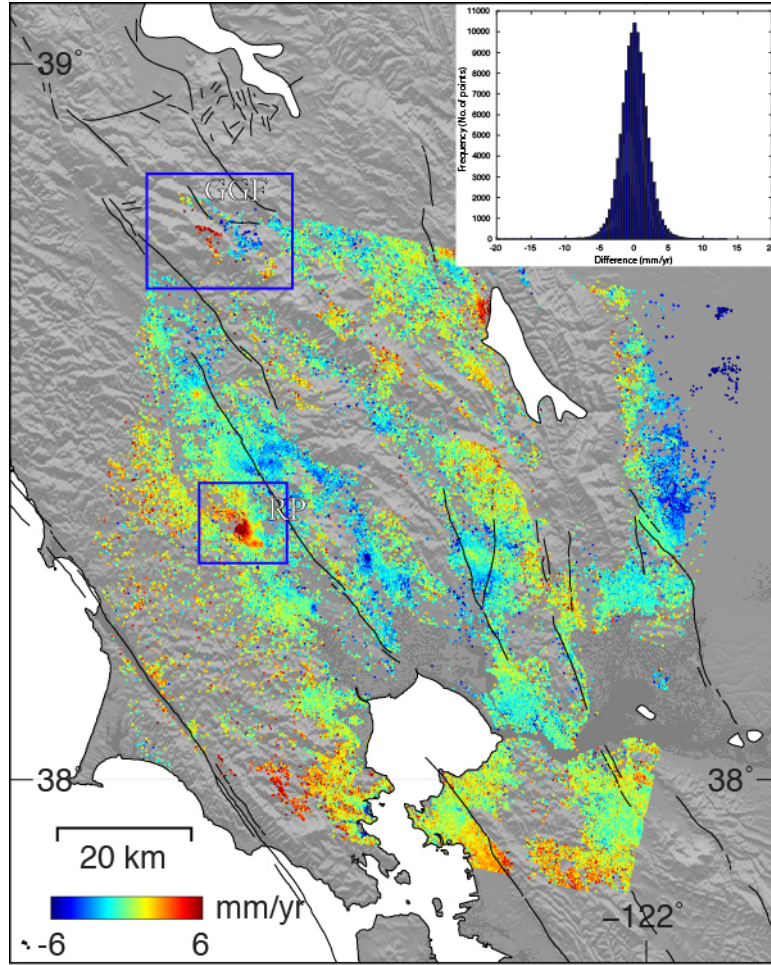


Figure S6. Difference between mean LOS velocity maps generated from descending 1992-2002 ERS-1/2 and 2006-2010 Envisat data. The disagreement in the Geysers geothermal region (GGF) and near Rohnert Park (RP) is probably due to the changed injection activity and recharging rate, respectively. The positive values in GGF suggests reduced subsidence rates, while the positive values in RP suggests more eastward motions during later period. The inset shows a histogram of the difference (standard deviation, 2 mm/yr).

Table S1 Information about the SAR data used in this study

Number	Envisat, Desc. Track 342		ERS, Desc. Track 342		Envisat, Asc. Track 478	
	Dates (yyyymmdd)	Baselines (m)	Dates (yyyymmdd)	Baselines (m)	Dates (yyyymmdd)	Baselines (m)
1	20060511	0	19920420	0	20061008	0
2	20060615	49.3767	19921116	-1317.0086	20061112	934.4834
3	20061207	182.0974	19930301	-546.6516	20061217	561.8523
4	20070705	-33.9618	19930405	-180.2049	20070715	382.4896
5	20070809	-105.8431	19930614	-1088.3686	20070819	655.0509
6	20070913	294.1843	19930823	-1300.3395	20071202	631.1547
7	20071122	104.6624	19950503	-1451.1739	20080106	303.7613
8	20071227	-286.5485	19950921	-864.6237	20080210	720.5923
9	20080131	96.0061	19951026	93.3049	20080316	483.6216
10	20080306	-299.7282	19951130	-1067.3213	20080525	348.5586
11	20080515	-66.8586	19960523	-890.1257	20080629	288.7792
12	20080619	154.4965	19970123	-734.0303	20080803	371.877
13	20080724	164.852	19970227	-795.1232	20081221	194.6488
14	20080828	74.9262	19970508	-947.288	20090125	625.5669
15	20090115	217.6964	19970612	-889.203	20090405	666.3262
16	20090219	19.3096	19970717	-901.1175	20090510	52.9362
17	20090430	-28.6074	19970821	-521.6628	20090614	91.0656
18	20090604	156.0121	19980319	-723.4324	20090719	324.3319
19	20090709	-51.3262	19980423	-587.3282	20090927	669.0633
20	20090813	10.1641	19990128	-744.567	20091101	244.2618
21	20090917	398.6114	19990304	-1943.468	20091206	707.2805
22	20091022	-76.5798	19990722	-194.8068	20100110	149.3179
23	20091231	-207.6102	19990826	-1568.4956	20100214	646.8591
24	20100204	434.4094	19990930	-350.6801	20100321	438.5826
25	20100311	-100.9845	20000914	-944.5121	20100530	428.121
26	20100415	220.9937	20001019	-638.1768	20100704	517.4135
27	20100520	100.8215	20001123	72.9825	20100808	160.5284
28	20100624	-9.186	20011213	-1307.3325	20100912	637.0882
29	20100902	36.8441	20020711	-1457.9614	20101017	962.4565
30	20101007	319.0497				

References

- Agram, P. S., and M. Simons (2015), A noise model for InSAR time series, *J. Geophys. Res. Solid Earth*, 120, 2752–2771, doi:10.1002/2014JB011271.
- Beeler, N. M., Lockner, D. L., and Hickman, S. H. (2001), A simple stick-slip and creep-slip model for repeating earthquakes and its implication for microearthquakes at Parkfield. *Bull. Seismol. Soc. Am.*, 91, 1797–1804.
- Borchardt, G., D. L. Snyder, C. J. Wills, Holocene slip rate of the Concord fault at Galindo Creek in Concord, California, final technical report, contract 1434-HQ-97-GR-03102, 30 pp., U.S. Geol. Surv., Menlo Park, Calif., 1999.
- Budding, K. E., Schwartz, D. P., and D. H. Oppenheimer (2012), Slip rate, earthquake recurrence, and seismogenic potential of the Rodgers Creek Fault Zone, northern California: Initial results, *Geophys. Res. Lett.*, 18, 447–450.
- Bürgmann, R., Schmidt, D., Nadeau, R. M., d'Alessio, M., Fielding, E., Manaker, D., McEvilly, T. V., and M. H. Murray (2000), Earthquake potential along the northern Hayward Fault, California, *Science*, 289, 1178–1182.
- Bürgmann, R., G. Hilley, A. Ferretti, and F. Novali (2006), Resolving vertical tectonics in the San Francisco Bay Area from permanent scatterer InSAR and GPS analysis, *Geology*, 34(3), 221, doi:10.1130/G22064.1.
- Çakir, Z., A. Akoglu, S. Belabbes, S. Ergintav, and M. Meghraoui (2005), Creeping along the ismetpasa section of the North Anatolian fault (western Turkey): Rate and extent from InSAR, *Earth Planet. Sci. Lett.*, 238(1–2), 225–234, doi:10.1016/j.epsl.2005.06.044.
- Chaussard, E., R. Bürgmann, M. Shirzaei, E. J. Fielding, and B. Baker (2014), Predictability of hydraulic head changes and characterization of aquifer-system and fault properties from InSAR-derived ground deformation, *J. Geophys. Res. Solid Earth*, 119, 6572–6590, doi:10.1002/2014JB011266.
- Chaussard, E., R. Bürgmann, H. Fattahi, C. W. Johnson, R. Nadeau, T. Taira, and I. Johanson (2015a), Interseismic coupling and refined earthquake potential on the Hayward-Calaveras fault zone, *J. Geophys. Res. Solid Earth*, 120, 8570–8590, doi:10.1002/2015JB012230.
- Chaussard, E., R. Bürgmann, H. Fattahi, R. M. Nadeau, T. Taira, C. W. Johnson, and I. Johanson (2015b), Potential for larger earthquakes in the East San Francisco Bay Area due to the direct connection between the Hayward and Calaveras Faults, *Geophys. Res. Lett.*, 42, 2734–2741, doi:10.1002/2015GL063575.
- d'Alessio, M. A., I. A. Johanson, R. Bürgmann, D. A. Schmidt, and M. H. Murray (2005), Slicing up the San Francisco Bay Area: Block kinematics and fault slip rates from GPS-derived surface velocities, *J. Geophys. Res.*, 110, B06403, doi:10.1029/2004JB003496.
- De Zan, F., M. Zonno, and P. López-Dekker (2015), Phase inconsistencies and multiple scattering in SAR interferometry, *IEEE Trans. Geosci. Remote Sens.*, 53, 6608–6616, doi:10.1109/TGRS.2015.2444431.
- Earthquake Engineering Research Institute (2015), M 6.0 South Napa earthquake of August 24, 2014, EERI Special Earthquake Report, California Earthquake Clearinghouse. [Available at <http://www.eqclearinghouse.org/2014-08-24-south-napa/preliminary-reports/#eeri-report>.]
- Erickson, B. A., Dunham, E. M., and Khosravifar, A. (2017), A finite difference method for off-

- fault plasticity throughout the earthquake cycle. *J. Mech. Phys. Solids*, 109, 50-77.
- Farr, T. G., et al. (2007), The Shuttle Radar Topography Mission, *Rev. Geophys.*, 45, RG2004, doi:10.1029/2005RG000183.
- Fattahi, H., and F. Amelung (2016), InSAR observations of strain accumulation and fault creep along the Chaman Fault system, Pakistan and Afghanistan, *Geophys. Res. Lett.*, 43, 8399–8406, doi:10.1002/2016GL070121.
- Feng, G., Z. Li, X. Shan, B. Xu, and Y. Du (2015), Source parameters of the 2014 Mw6.1 South Napa earthquake estimated from the Sentinel 1A, COSMO-SkyMed and GPS data, *Tectonophysics*, 655, 139–146.
- Ferretti, A., F. Novali, R. Bürgmann, G. Hilley, and C. Prati (2004), InSAR permanent scatterer analysis reveals ups and downs in San Francisco Bay Area, *Eos Trans. AGU*, 85(34), 317–324, doi:10.1029/2004EO340002.
- Ferretti, A., A. Fumagalli, F. Novali, C. Prati, F. Rocca, and A. Rucci (2011), A new algorithm for processing interferometric data-stacks: SqueeSAR, *IEEE Trans. Geosci. Remote Sens.*, 49(9), 3460-3470, doi:10.1109/TGRS.2011.2124465.
- Field, E. H., et al. (2015), Long-term time-dependent probabilities for the Third Uniform California Earthquake Rupture Forecast (UCERF3), *Bull. Seismol. Soc. Am.*, 105(2A), 511–543, doi:10.1785/0120140093.
- Floyd M. A. and G. J. Funning, (2013), Continuation of survey GPS measurements and installation of continuous GPS sites at The Geysers, California, for geothermal deformation monitoring, *Geothermal Resources Council Trans.*, 37, 895-898.
- Floyd, M. A., et al. (2016), Spatial variations in fault friction related to lithology from rupture and afterslip of the 2014 South Napa, California, earthquake, *Geophys. Res. Lett.*, 43, 6808–6816, doi:10.1002/2016GL069428.
- Fornaro, G., A. Pauciuillo, and D. Reale (2011), A null-space method for the phase unwrapping of multitemporal SAR interferometric stacks, *IEEE Trans. Geosci. Remote Sens.*, 49, 2323-2334, doi:10.1109/TGRS.2010.2102767.
- Freymueller, J. T., M. H. Murray, P. Segall, and D. Castillo (1999), Kinematics of the Pacific-North America Plate Boundary Zone, northern California, *J. Geophys. Res.*, 104(B4), 7419–7441, doi:10.1029/1998JB900118.
- Funning, G. J., R. Bürgmann, A. Ferretti, F. Novali, and A. Fumagalli (2007), Creep on the Rodgers Creek fault, northern San Francisco Bay area, from a 10-year PS-InSAR dataset, *Geophys. Res. Lett.*, 34, L19306, doi:10.1029/2007GL030836.
- Galehouse, J. S., and J. J. Lienkaemper (2003), Inferences drawn from two decades of alignment array measurements of creep on faults in the San Francisco Bay region, *Bull. Seismol. Soc. Am.*, 93(6), 2415–2433.
- Hanssen, R. F. (2001), *Radar interferometry: Data interpretation and error analysis*, Springer Science and Business Media.
- Hecker, S., et al. (2005), The most recent large earthquake on the Rodgers Creek fault, San Francisco Bay Area, *Bull. Seismol. Soc. Am.*, 95, 844–860.

- Hecker, S., V. E. Langenheim, R. A. Williams, C. S. Hitchcock, and S. B. DeLong (2016), Detailed mapping and rupture implications of the 1 km releasing bend in the Rodgers Creek fault at Santa Rosa, northern California, *Bull. Seismol. Soc. Am.*, *106*, 575–594, doi:10.1785/0120150152.
- Herring, T.A., R.W. King, S.C. McClusky (2010a), GAMIT Reference Manual. Release 10.4. Mass. Inst. of Technol., Cambridge.
- Herring, T.A., R.W. King, S.C. McClusky (2010b), GLOBK Reference Manual. Release 10.4. Mass. Inst. of Technol., Cambridge.
- Jin, L., and G. J. Funning (2017), Testing the inference of creep on the northern Rodgers Creek fault, California, using ascending and descending persistent scatterer InSAR data, *J. Geophys. Res. Solid Earth*, *122*, 2373–2389, doi:10.1002/2016JB013535.
- Jolivet, R., C. Lasserre, M.-P. Doin, S. Guillaso, G. Peltzer, R. Dailu, J. Sun, Z.-K. Shen, and X. Xu (2012), Shallow creep on the Haiyuan Fault (Gansu, China) revealed by SAR Interferometry, *J. Geophys. Res.*, *117*, B06401, doi:10.1029/2011JB008732.
- Lienkaemper, J. J., F. S. McFarland, R. W. Simpson, and S. J. Caskey (2014), Using surface creep rate to infer fraction locked for sections of the San Andreas fault system in Northern California from alignment array and GPS data, *Bull. Seismol. Soc. Am.*, *104*, 3094–3114, doi:10.1785/0120140117.
- Lin, Y. N., M. Simons, E. A. Hetland, P. Muse, and C. DiCaprio (2010), A multiscale approach to estimating topographically correlated propagation delays in radar interferograms, *Geochem. Geophys. Geosyst.*, *11*, Q09002, doi:10.1029/2010GC003228.
- Marinkovic, P., and Y. Larsen (2013), Consequences of long-term ASAR local oscillator frequency decay—An empirical study of 10 years of data, Proceedings of the Living Planet Symposium, European Space Agency, Edinburgh, U. K.
- McFarland, F. S., J. J. Lienkaemper, and S. J. Caskey, (2016), Data from theodolite measurements of creep rates on San Francisco Bay region faults, California, U.S. Geol. Surv. Open File Rep., 2009–1119, Menlo Park, Calif.
- McPhee, D. K., V. E. Langenheim, and R. C. Jachens (2007), Basin structure beneath the Santa Rosa Plain, northern California: Implications for damage caused by the 1969 Santa Rosa and 1906 San Francisco earthquakes, *Bull. Seismol. Soc. Am.*, *97*, 1449–1457.
- Metzger, S. and S. Jónsson (2014), Plate boundary deformation in North Iceland during the 1992–2009 revealed by InSAR time-series analysis and GPS, *Tectonophysics*, *634*, 127–138.
- Monti-Guarnieri, A. and S. Tebaldini (2008), On the exploitation of target statistics for SAR interferometry applications, *IEEE Trans. Geosci. Remote Sens.*, *46*(11), 3436–3443, doi:10.1109/TGRS.2008.2001756.
- Mossop, A., and P. Segall (1997), Subsidence at The Geysers Geothermal Field, N. California from a comparison of GPS and leveling surveys, *Geophys. Res. Lett.*, *24*(14), 1839–1842, doi:10.1029/97GL51792.
- Murray, J. R., S. E. Minson, and J. L. Svarc (2014), Slip rates and spatially variable creep on faults of the northern San Andreas system inferred through Bayesian inversion of Global Positioning System data, *J. Geophys. Res. Solid Earth*, *119*, 6023–6047, doi:10.1002/2014JB010966.

- Murray, J.R. and J. Svarc. (2017), Global Positioning System data collection, processing, and analysis conducted by the U.S. Geological Survey Earthquake Hazards Program, *Seismol. Res. Lett.*, 88, 916-925, doi:10.1785/0220160204.
- Nadeau, R. M., and T. V. McEvilly (1999), Fault slip rates at depth from recurrence intervals of repeating microearthquakes, *Science*, 285(5428), 718-721, doi:10.1126/science.285.5428.718.
- Nadeau, R. M., and T. V. McEvilly (2004), Periodic pulsing of characteristic microearthquakes on the San Andreas Fault, *Science*, 303, 220-222, doi:10.1126/science.1090353.
- NCEDC (2014), Northern California Earthquake Data Center. UC Berkeley Seismological Laboratory. Dataset, doi:10.7932/NCEDC.
- Niemi, T. M., and N.T. Hall (1992), Late Holocene slip rate and recurrence of great earthquakes on the San Andreas fault in northern California, *Geology*, 20(3), 195-198.
- Pepe, A., and R. Lanari (2006), On the extension of the minimum cost flow algorithm for phase unwrapping of multitemporal differential SAR interferograms, *IEEE Trans. Geosci. Remote Sens.*, 44(9), 2374-2383, doi:10.1109/TGRS.2006.873207.
- Prescott, W. H., J. C. Savage, J. L. Svarc, and D. Manaker (2001), Deformation across the Pacific-North America plate boundary near San Francisco, California, *J. Geophys. Res.*, 106(B4), 6673-6682, doi:10.1029/2000JB900397.
- Rocca, F. (2007), Modeling interferogram stacks, *IEEE Trans. Geosci. Remote Sens.*, 45(10), 3289-3299, doi:10.1109/TGRS.2007.902286.
- Rowshandel B., Reichle M., Wills C., Cao T., Petersen M., Branum D., Davis J. Estimation of Future Earthquake Losses in California California Geological Survey, Menlo Park, California (2006)
- Ryder, I. and R. Bürgmann (2008), Spatial variations in slip deficit on the central San Andreas Fault from InSAR. *Geophys. J. Int.*, 175, 837-852, doi:10.1111/j.1365-246X.2008.03938.x.
- Schmidt, D. A., R. Bürgmann, R. M. Nadeau, and M. d'Alessio (2005), Distribution of aseismic slip rate on the Hayward fault inferred from seismic and geodetic data, *J. Geophys. Res.*, 110, B08406, doi:10.1029/2004JB003397.
- Shirzaei, M., and R. Bürgmann (2013), Time-dependent model of creep on the Hayward fault from joint inversion of 18 years of InSAR and surface creep data, *J. Geophys. Res. Solid Earth*, 118, 1733-1746, doi:10.1002/jgrb.50149.
- Shirzaei, M., and R. Bürgmann (2018), Global climate change and local land subsidence exacerbate inundation risk to the San Francisco Bay Area, *Sci. Adv.*, 4, eaap9234, doi:10.1126/sciadv.aap9234.
- Thatcher, W., G. Marshall, and M. Lisowski (1997), Resolution of fault slip along the 470-km-long rupture of the great 1906 San Francisco earthquake and its implications, *J. Geophys. Res.*, 102, 5353-5367, doi:10.1029/96JB03486.
- Tong, X., D. T. Sandwell, and B. Smith-Konter (2013), High-resolution interseismic velocity data along the San Andreas Fault from GPS and InSAR, *J. Geophys. Res. Solid Earth*, 118, 369-389, doi:10.1029/2012JB009442.
- Turner, R. C., R. M. Nadeau, and R. Bürgmann (2013), Aseismic slip and fault interaction from

- repeating earthquakes in the Loma Prieta aftershock zone, *Geophys. Res. Lett.*, *40*, 1079–1083, doi:10.1002/grl.50212.
- Vasco, D. W., et al. (2013), Monitoring deformation at The Geysers Geothermal Field, California using C-band and X-band interferometric synthetic aperture radar, *Geophys. Res. Lett.*, *40*, 2567–2572, doi:10.1002/grl.50314.
- Wong, I. G., and J. D. J. Bott (1995), A new look back at the 1969 Santa Rosa, California, earthquakes, *Bull. Seismol. Soc. Am.*, *85*(1), 334–341.
- Wright, T., B. Parsons, and E. Fielding (2001), Measurement of interseismic strain accumulation across the North Anatolian Fault by satellite radar interferometry, *Geophys. Res. Lett.*, *28*, 2117–2120, doi:10.1029/2000GL012850.
- Xu, W., Wu, S., Materna, K., Nadeau, R., Floyd, M., Funning, G., Chaussard, E., Johnson, C. , Murray, J. , Ding, X. , and Bürgmann, R. (2018). Interseismic ground deformation and fault slip rates in the greater San Francisco Bay Area from two decades of space geodetic data. *Journal of Geophysical Research: Solid Earth*, *123*, doi: 10.1029/2018JB016004.
- Zhang, L., X. Ding, and Z. Lu (2011), Modeling PSInSAR time series without phase unwrapping, *IEEE Trans. Geosci. Remote Sens.*, *49*, 547-556, doi:10.1109/TGRS.2010.2052625.